

# Stars, H II regions, and shocked gas in the bar of NGC 1530

A. Greve, D. Reynaud, and D. Downes

Institut de Radio Astronomie Millimétrique, F-38406 St. Martin d'Hères, France

Received 26 October 1998 / Accepted 4 June 1999

**Abstract.** We analyse long slit spectra taken along and perpendicular to the bar of the galaxy NGC 1530. Our data show that the H II regions, around young massive stars that form in the shock-compressed gas, share the same kinematics as the molecular gas in the  $x_2$  orbits at the center of the galaxy. Along the bar, the H II regions are in the post-shock zone, downstream of the dust lanes that contain molecular gas. Outside of the H II regions in the bar is faint, diffuse, ionized gas with a low  $H\alpha / [NII]$  and  $H\alpha / [SII]$  line ratio, which confirms the presence of shocks in the bar and supports a shock origin of the dust lanes. The measured spatial variation of the  $H\alpha$  and  $[NII]$  line intensity is consistent with the distribution of molecular gas along the dust lanes and its high concentration near the first inner Lindblad resonance. From an  $I - B$  image, we derive the surface brightness along the bar which we interpret as the stellar distribution. We use these data to estimate the mass in the various structural components of the bar. The mass of the stars and gas in the bar is  $4 \times 10^{10} M_{\odot}$ , or 12% of the total mass of the galaxy.

**Key words:** galaxies: individual: NGC 1530 – galaxies: ISM – galaxies: kinematics and dynamics – galaxies: structure

## 1. Introduction

### 1.1. Bar shocks and dust lanes in model simulations

The stars in galaxy bars move on elliptical orbits along the bar, or  $x_1$  orbits in the notation introduced by Contopoulos & Mertzaniades (1977). Near the inner Lindblad resonance, the orbits become perpendicular to the bar ( $x_2$  orbits). If the rotation curve allows a second inner Lindblad resonance, closer to the nucleus, the orbits inside this resonance return to the  $x_1$  shape, with major axes along the bar. Because of dissipation of kinetic energy into heat and radiation, the motion of the dust and gas is expected to differ from that of the stars.

Barred galaxies have dust lanes that start near their centers and follow the leading edges of the bar out to, or even into the spiral arms. In gas-dynamic simulations, the dust lanes of barred galaxies appear as high-density, shock-compressed regions with complex motions. Gas flows along the  $x_1$  orbits toward the galactic center. Near the center it hits the gas on the  $x_2$

orbits and the resulting shock produces regions of dense, compressed gas. After this shock, the flow traverses the inside of the bar until it hits the gas stream flowing in the opposite direction on the other side of the bar. This produces secondary shocks, on the leading edges of the bar, which are the long, straight dust lanes seen on optical images (e.g., Roberts et al. 1979; Athanasoulas 1992; Piner et al. 1995; Lindblad et al. 1996b; Lindblad & Kristen 1996; Englmaier & Gerhard 1997). The simulations predict an increasing shock strength toward the center of the bar, with the strongest shocks occurring at the intersection of the  $x_1$  and  $x_2$  orbits near the first inner Lindblad resonance. The shocks compress the diffuse interstellar gas. If the shear across the shocks is not too strong, the compression may yield sufficiently high densities for the formation of massive stars and their H II regions, as seen along many bars.

### 1.2. Observational evidence for bar shocks

Evidence for bar shocks is obtained from observations of molecular gas, radio continuum emission, velocity jumps, and emission-line ratios.

For some galaxies with large bars longer than 5 kpc, the dense, shock-compressed gas of the long, straight dust lanes is detectable in CO. The best evidence for molecular gas in the dust lanes of galaxies with large bars are the interferometer maps of CO in NGC 7479 by Quillen et al. (1995) and in NGC 1530 by Downes et al. (1996; hereafter DRSR) and Reynaud & Downes (1998; hereafter RD98).

For several barred galaxies, the predicted compression in the dust lanes is confirmed by radio continuum maps, such as those of NGC 1097 (Ondrechen & van der Hulst 1983), M 83 (Ondrechen 1985), NGC 1365 (Sandqvist et al. 1995), and NGC 1530 (Condon et al. 1996; Regan et al. 1996). These maps indicate enhanced synchrotron radiation in the dust lanes, corresponding to higher magnetic fields (Beck et al. 1999) and increased acceleration of relativistic particles in shocks.

The expected velocity jumps across the shocked dust lanes have been seen in a few barred galaxies. In NGC 6221, Pence & Blackman (1984) detected in  $H\alpha$  a velocity jump of  $150 \text{ km s}^{-1}$  over a distance  $\leq 200 \text{ pc}$ . Weiner et al. (1993) report a  $100$  to  $150 \text{ km s}^{-1}$  jump over the  $3''$ -wide dust lanes in NGC 3095, and Weiner et al. (1996) report velocity jumps across the dust lanes in the bar of NGC 4123. Similar jumps can be seen across the

dust lanes of NGC 1365 in the spectra 12, 14, 17, 18, and 24 of Lindblad et al. (1996a).

In the low-density interstellar gas the velocity jumps at the bar shocks are  $\gtrsim 100 \text{ km s}^{-1}$ , high enough to produce “photoionizing shocks”. These hot shocks collisionally excite heavy ions and produce enough photons to ionize the preshock region upstream from the shock and to maintain the ionization of the cooling gas downstream from the shock. For recent shock models see Dopita & Sutherland (1995; 1996) and Morse et al. (1996). These excitation processes yield optical emission line ratios different from those of H II regions and comparable with those in old supernova remnants, like the Cygnus Loop, where the velocity jumps and densities are similar (e.g., Osterbrock 1989). In particular, the  $\text{H}\alpha/[\text{NII}]$ ,  $\text{H}\alpha/[\text{SII}]$ , and  $\text{H}\alpha/[\text{OII}]$  line ratios are closer to unity, rather than their usual values of 2 to 5 in H II regions (e.g., Burbidge et al. 1963; Osterbrock 1989). The ratios of these lines may thus be used as tracers of shocked gas. The  $\text{H}\alpha$  (6563 Å),  $[\text{NII}]$  (6548, 6583 Å), and  $[\text{SII}]$  (6716, 6731 Å) lines are well suited for such studies because they are easy to measure and their wavelengths are nearly the same.

There is a long history of observations of low  $\text{H}\alpha/[\text{NII}]$  6583 line ratios in barred galaxies (e.g., Burbidge & Burbidge 1962; 1965; Rubin et al. 1980). Examples of studies showing the low ratios in the diffuse gas *along the bars*, well outside the nucleus, are by Duval (1977; for NGC 5838), Storchi-Bergmann et al. (1996; for NGC 1097, NGC 1672, and NGC 5248), and Marquez et al. (1996; for NGC 6701).

### 1.3. Bar shocks in NGC 1530

The galaxy NGC 1530 has an enormous bar, 24 kpc long, and striking dust lanes that leave the nucleus in opposite directions and follow the major axis of the bar out to the spiral arms. The molecular gas along the bar – the  $x_1$  orbit zone – and in the nuclear ring and at the center of the bar – the  $x_2$  orbit zone – has been observed in CO by Downes et al. (1996; DRSR), Reynaud & Downes (RD97; RD98), and Regan et al. (1995, 1996). Regan et al. (1997) analysed Fabry-Perot  $\text{H}\alpha$  observations and derived a mass inflow rate from the dust lanes to the nuclear ring of  $1 M_{\odot} \text{ yr}^{-1}$ .

In this paper we describe optical emission line data from long slit spectroscopy of the H II regions and the diffuse ionized gas. We analyse the low  $\text{H}\alpha/[\text{NII}]$  and  $\text{H}\alpha/[\text{SII}]$  line ratios near the dust lanes, which indicate excitation by shocks. We derive from an  $I - B$  image the stellar surface brightness distribution. We use this brightness distribution together with the dynamical mass in the central region – calculated from rotation velocities – to estimate the mass of the stars in the  $x_1$  and  $x_2$  orbits and the nuclear bulge.

## 2. Observations

The line of nodes of NGC 1530 is at p.a.  $19^\circ$  east of north. The long axis of the bar is at p.a.  $115^\circ$ , i.e., nearly east-west. The galaxy is inclined by  $55^\circ$  around the line of nodes (Grosbol 1985;  $90^\circ = \text{edge-on}$ ). The uncertainty of the inclination

of  $\sim \pm 5^\circ$  introduces an uncertainty of  $\sim \pm 5\%$  in the deprojected velocities and an uncertainty of  $\sim \pm 15\%$  in the dynamical mass ( $\propto v^2$ ). At 37 Mpc distance,  $1''$  is 180 pc along this line of nodes (approximately perpendicular to the bar), and 310 pc along the bar. Whenever we quote linear distances (pc) they are true, deprojected distances. All velocity offsets are relative to  $c z_{\text{lsr}} = 2450 \text{ km s}^{-1}$ . For further parameters of NGC 1530 see DRSR (1996).

The observations were made in service time with the 2.5 m Isaac Newton Telescope of the Royal Greenwich Observatory, on La Palma, Spain. The spectrometer slit had dimensions of  $5 \text{ arcmin} \times 1.5 \text{ arcsec}$ . In a first exposure the slit was aligned at p.a.  $110^\circ$ , within  $\pm 1''$  through the center of NGC 1530, and parallel and close to the dust lanes. In a second exposure, the slit was shifted  $4''$  (0.7 kpc) north. This slit orientation is parallel to the bar, along the  $x_1$  orbits, and nearly orthogonal to the  $x_2$  orbits and the line of nodes of the galaxy (DRSR 1996; RD97). In a third exposure, the slit passed through the center at p.a.  $200^\circ$ , perpendicular to the bar, and nearly along the  $x_2$  orbits and the galaxy’s line of nodes. On the position axis of the spectrogram, the pixels were spaced every  $0.8''$  (145 pc perpendicular to the bar, 250 pc along the bar). The seeing was about the same order as the spatial sampling.

Each spectrum covered  $\text{H}\alpha$  at 6563 Å,  $[\text{NII}]$  at 6548, 6583 Å and  $[\text{SII}]$  at 6716, 6731 Å. We used a 1200 line/mm grating which gave a spectral sampling of  $0.8 \text{ \AA/pixel}$ , or  $35 \text{ km s}^{-1}/\text{pixel}$ . The instrumental resolution (FWHM) was determined from faint sky emission lines to be  $110 \text{ km s}^{-1}$ . The exposures were bias-corrected and flat-fielded in the usual way.

The analysis of faint diffuse emission requires a reliable subtraction of the sky background and of the stellar continuum. The high spectral dispersion gave good measures of the background,  $B_-$  and  $B_+$ , on both sides of a spectral line. The corrected  $\text{H}\alpha$  line, for example, is  $\text{H}\alpha_{\text{corr}} = (\text{H}\alpha + B)_{\text{obs}} - (B_- + B_+)/2$ . The redshifted  $\text{H}\alpha$ ,  $[\text{NII}]$ , and  $[\text{SII}]$  lines of NGC 1530 are not blended by atmospheric emission lines, but they are superposed on a weak, composite spectrum of late-type stars in the bar, and would normally require a correction for the stellar photospheric  $\text{H}\alpha$  absorption line. At positions where the bar’s H II region and diffuse emission is weak, we found no trace of *broad*  $\text{H}\alpha$  absorption, and therefore made no correction.

From the spectroscopic data we obtained relative  $\text{H}\alpha$ ,  $[\text{NII}]$  6583 and  $[\text{SII}]$  emission intensities and derived the  $\text{H}\alpha/[\text{NII}]$  6583,  $\text{H}\alpha/[\text{SII}]$  6716, and  $[\text{SII}]$  6716/6731 line ratios. We used an  $I$ -band image ( $\lambda_0 = 8800 \text{ \AA}$ ,  $\Delta\lambda = 2200 \text{ \AA}$ ) and  $B$ -band image ( $\lambda_0 = 4400 \text{ \AA}$ ,  $\Delta\lambda = 1000 \text{ \AA}$ ), taken with the 2.2 m telescope at Calar Alto, Spain, at  $\sim 1.5''$  seeing, to derive the distribution of stellar surface brightness along the bar.

## 3. Results for the gas

### 3.1. The ionized gas of the bar

Figs. 1 and 2 summarize our observations. Fig. 1 shows the spectra along the bar, which is nearly orthogonal to the galaxy’s line of nodes. *Column A (left)* is with the slit passing within  $\pm 1''$  through the galactic center, *Column B (right)* is with the

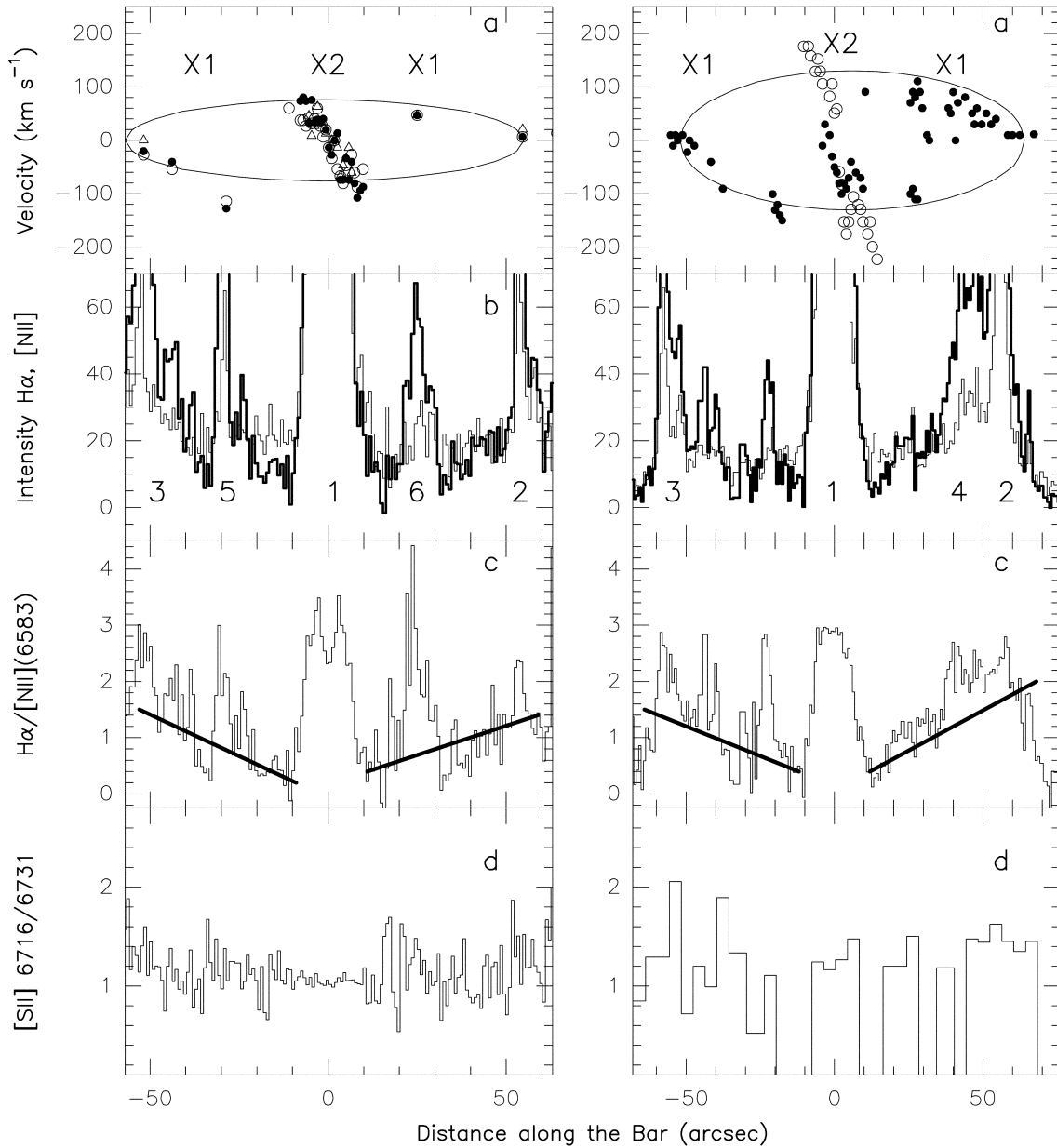


**Fig. 1a–d.** Line-of-sight velocity, line intensities, and line ratios **along** the bar in NGC 1530. Southeast is left, northwest is right. (A), *left column*: slit at p.a.  $110^\circ$ , through the center of the galaxy. (B), *right column*: slit parallel to (A) but shifted  $4''$  north. **a:** Radial velocities, relative to  $2450 \text{ km s}^{-1}$ , measured from  $\text{H}\alpha$  (solid dots),  $[\text{NII}]$  (open circles), and  $[\text{SII}]$  (triangles). The  $x_1$  and  $x_2$  orbit families are indicated schematically. **b:** Relative intensity of  $\text{H}\alpha$  (heavy line) and  $[\text{NII}]$  (thin line) in linear counts. Bright H II region complexes are numbered as in Regan et al. (1996). **c:** Line ratio  $\text{H}\alpha / [\text{NII}] 6583$ . The heavy lines trace the line ratio of the shocked, diffuse ionized gas. **d:**  $[\text{SII}]$  line ratio. Along the bar,  $1'' \leftrightarrow 310 \text{ pc}$  deprojected.

slit shifted  $4''$  north. Fig. 1a shows the line-of-sight velocity along the slit, derived from the  $\text{H}\alpha$ ,  $[\text{NII}]$ , and  $[\text{SII}]$  emission lines, as well as a sketch of the  $x_1$  and  $x_2$  orbit families. Fig. 1b gives the relative intensities of the  $\text{H}\alpha$  and  $[\text{NII}] 6583$  lines. The  $[\text{NII}] 6548$  line intensity (not shown) is  $1/3$ rd that of the  $[\text{NII}] 6583$  line. The plots emphasize the weak diffuse gas between the main H II regions. Fig. 1c gives the  $\text{H}\alpha / [\text{NII}] 6583$  line ratio which serves as a tracer of the excitation – a value of  $\sim 3$  indicates H II regions and photo-ionization by OB stars, a value  $\lesssim 1$  indicates excitation in shocks. Fig. 1d gives the

$[\text{SII}] 6716 / 6731$  line ratio; its value of  $\sim 1.4$  indicates a low electron density of the ionized gas.

Fig. 2 shows the same quantities as Fig. 1, but with the slit perpendicular to the bar, which is nearly the galaxy’s line of nodes. In this slit position, there is emission only in the galactic center (region 1 in Fig. 1b). Fig. 2 also gives the CO position-velocity curve, from RD97.

To interpret the NGC 1530 kinematics, RD97 adopted a pattern speed of  $17 \text{ km s}^{-1} \text{ kpc}^{-1}$ , and derived a rotation curve. This yielded the first inner Lindblad resonance at a radius of

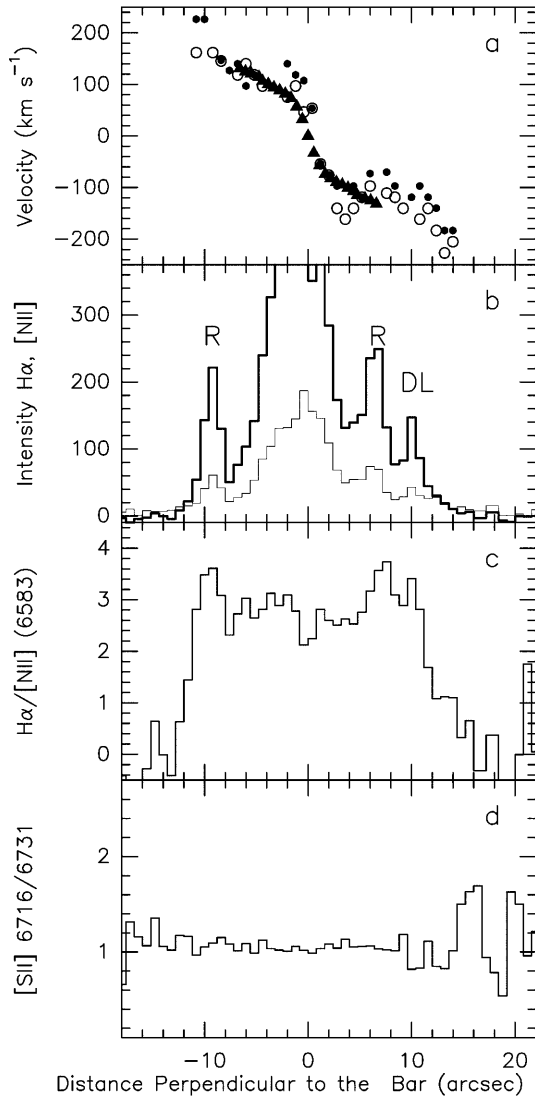


**Fig. 2a–d.** Line-of-sight velocity, line intensity, and line ratios **perpendicular** to the bar in NGC 1530. The slit is at p.a.  $200^\circ$ , and passes through the galactic center. South is left, north is right. **a**  $H\alpha$ : solid dots,  $[NII]$ : open circles, average velocity of CO: solid triangles (taken from RD97). **b** The positions marked *R* indicate a ring of ionized material near the first inner Lindblad resonance (see Fig. 4), *DL* indicates the northern dust lane. Other symbols and units as in Fig. 1. On the bar’s minor axis,  $1'' \leftrightarrow 180$  pc.

$\sim 1.4$  kpc, and the second inner Lindblad resonance at a radius  $\sim 0.15$  kpc. Co-rotation occurs at a radius of 14 kpc, just beyond the far ends of the bar. The outer Lindblad resonance is near the outer ends of the spiral arms. (Since the motions in the bar have significant non-circular components, the locations of “resonances” are of course somewhat diffuse.)

### 3.2. Kinematics of the central H II regions ( $r \leq 2$ kpc)

From our data we see that intense H II regions extend  $\pm 8''$  and  $\pm 12''$  from the center along and perpendicular to the bar, respectively (Figs. 1 & 2b). The deprojected zone is nearly circu-

lar, with an outer radius of 2 kpc. A similar central plateau of CO emission and patchy HCN emission was found by DRSR (1996) and RD97. The main emission of the H II zone peaks close to the predicted 1.4 kpc radius of the inner Lindblad resonance (RD97), while the radius to zero intensity extends to 2 kpc. Throughout this zone the  $H\alpha/[NII]$  6583 ratio is 2.5 to 3, typical of H II regions (Figs. 1 & 2c).

Fig. 3 shows the position-velocity diagram along the bar (p.a.  $110^\circ$ ) of the H II regions (from Fig. 1) and of the molecular gas (from DRSR 1996, RD97). Like the molecular gas, the ionized gas inside the central region follows the  $x_2$  orbits (Figs. 1a & 3). In these diagrams (Fig. 1), the  $x_2$  streamlines are not exactly perpendicular to the  $x_1$  orbits but are shifted  $\sim 20^\circ$  to the east, as found by DRSR (1996) in the molecular gas. There is a remarkably low scatter in the velocities of both the molecular gas and the H II regions, indicating that the gas motion and the motion of *young* stars must be rather stable and not significantly disturbed by shocks.

One of the few barred galaxies in which both gas and star kinematics have been measured is NGC 6221, which resembles NGC 1530 in type, size, orientation, and distance. In this galaxy, the velocities of the stars and gas on the  $x_2$  orbits are the same (Vega Beltran et al. 1998). Although we have no velocity data for the stars, we think the stars in NGC 1530 follow the  $x_2$  orbits as well.

### 3.3. The inner Lindblad resonance ( $r \sim 1.5$ kpc)

Fig. 4 shows the  $H\alpha$  and  $[NII]$  intensity of H II regions along and perpendicular to the bar. A ring of H II regions with a  $H\alpha/[NII]$  6583 line ratio  $\approx 3$  appears at a radius of 1.5 kpc, the same as the radius of the first inner Lindblad resonance predicted from the kinematic analysis. The width of the ring is 200 to 300 pc. The enhanced  $H\alpha$  and  $[NII]$  emission indicates an increased density of young, massive stars and their H II regions (Fig. 4). A similar ring of gas located near the first inner Lindblad resonance is observed in the barred galaxy NGC 6221 (Vega Beltran et al. 1998; Koribalski 1996).

In a cut through the center of the bar, the  $H\alpha$  and  $[NII]$  profiles have two velocity peaks (Fig. 5), separated by  $140$  km s $^{-1}$  at a radius of  $2''$  (630 pc) along the bar. The  $H\alpha/[NII]$  6583 line ratios in the two peaks are 2 to 3, typical of H II regions (Fig. 5). The velocities of the twin peaks are close to those of the two main velocity components of the  $x_2$  orbits at 2350 and 2500 km s $^{-1}$ , nearly the same as those of the main CO peaks in the high-resolution CO(2–1) channel maps of Reynaud & Downes (1999). The positive velocity peak corresponds to the  $x_2$  orbit velocities to the south of the galactic center, and the negative velocity peak corresponds to the  $x_2$  orbit velocities north of the galactic center.

The relation of these two minor peaks in velocity to the larger-scale position-velocity diagram along the bar is shown in Fig. 6. In the position-velocity diagrams in  $H\alpha$  and CO, the intensity is greatest on the southeast and northwest sides of the  $x_2$  orbits, separated by  $8''$  (2.5 kpc). Exactly at the center of the bar (the dashed vertical line in the  $H\alpha$  diagram in Fig. 6), the

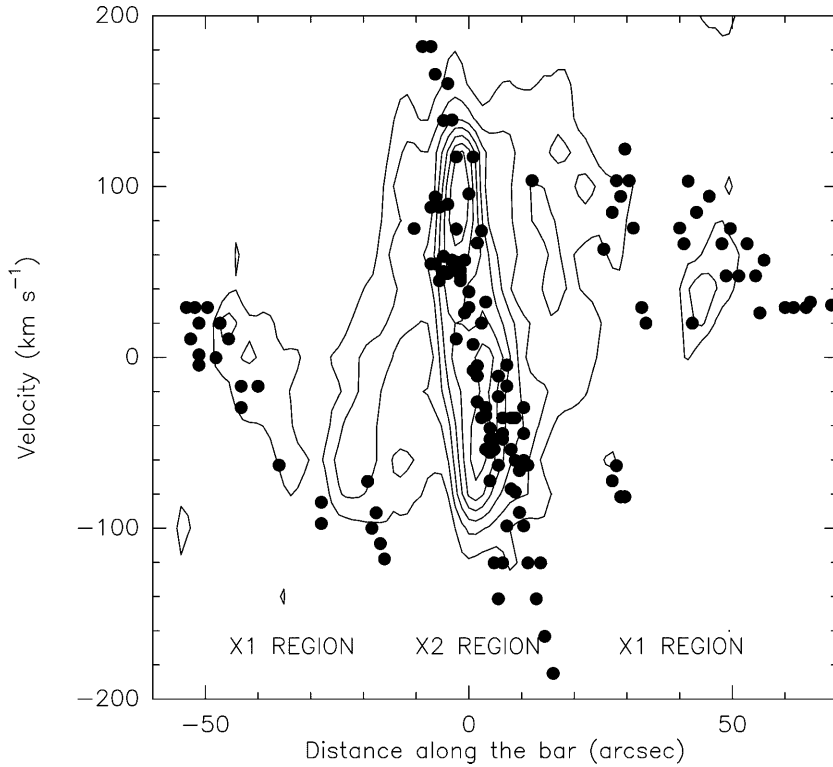


**Fig. 3.** Position-velocity diagram along the bar, of H $\alpha$  and [NII] emission from H II regions (dots; from Fig. 1) and  $^{12}\text{CO}(1-0)$  emission from molecular gas (contour interval is  $30 \text{ mJy beam}^{-1}$ ; data from RD98). The zero of the velocity scale is  $cz_{\text{lsr}} = 2450 \text{ km s}^{-1}$ . The molecular gas is in the  $x_2$  region and in the shocked zones on the leading  $x_1$  orbits (Fig. 1a). The H II regions are in the  $x_2$  region and in the post-shock zones, slightly downstream of the  $x_1$  molecular gas. Left is southeast, right is northwest, and  $1''$  corresponds to  $310 \text{ pc}$ . The zero position is  $04^{\text{h}}23^{\text{m}}26.73^{\text{s}}, +75^{\circ}17'44.0''$  (J2000).

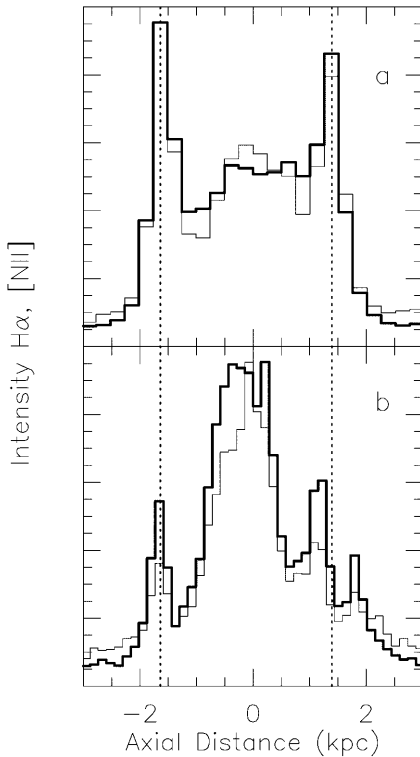


**Fig. 4a and b.** Ionized gas in the  $x_2$  region (linear counts scaled to peak intensities). **a** H $\alpha$  (thick line) and [NII] (thin line) intensity along the bar. Left is southeast, right is northwest. **b** H $\alpha$  (thick line) and [NII] (thin line) intensity perpendicular to the bar. Left is south, right is north. The vertical dashed lines indicate a partial ring of enhanced emission near the first inner Lindblad resonance.

$x_2$  orbits yield two minor peaks – the twin peaks in Fig. 5. A similar effect is seen in CO, and results from the bar not being perpendicular to the line of nodes, but at a  $96^\circ$  angle to it. This causes two velocity components within the aperture, but they are normal components of the nearly circular rotation in the  $x_2$  orbits.

#### 3.4. The H II regions along the bar ( $r > 2 \text{ kpc}$ )

Further out, at radii  $> 2 \text{ kpc}$  from the center, there are several bright H II regions along the bar (Fig. 1b), with a H $\alpha$  / [NII] 6583 line ratio of 2 to 3. In the position-velocity diagram, these H II regions are slightly displaced from the molecular gas (Fig. 3). The molecular gas is in the dust lanes at the leading  $x_1$  orbits (DRSR 1996), the zones of the strongest gas compression by the bar-induced shocks.

The position of the molecular gas (CO) and the ionized gas (H $\alpha$ ) shown in Fig. 3 suggests that beyond the first inner Lindblad resonance the H II regions are in the post-shock zones slightly downstream of the molecular gas. The likely sequence of massive star formation is passage of the shock, compression of the gas, cooling of the dense gas, formation of OB stars, decompression of the gas, and expansion and full development of the H II regions. The separation of the H II regions from the most intense lanes of molecular gas is about  $5''$  or  $1.5 \text{ kpc}$  on the bar's major axis. If the relative velocity of the shock and the newly formed stars is  $100 \text{ km s}^{-1}$ , then the time between the passage of the density-wave shock and the dissipation of the molecular clouds and the full development of the H II regions with stellar clusters would be about  $1 \times 10^7 \text{ yr}$  ( $\approx 1.5 \text{ kpc} / 100 \text{ km s}^{-1}$ ),

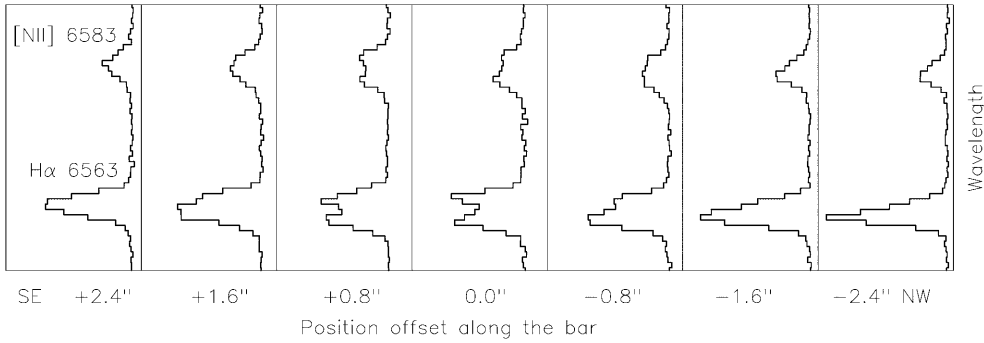


**Fig. 5.** Split emission lines along the bar's long axis. The spectra are spaced by 1 pixel, or  $0.8''$ ; southeast is left, northwest is right. Negative velocity offsets are down, positive velocities are up. One spectral pixel of  $0.8 \text{ \AA}$  corresponds to a spectral sampling  $35 \text{ km s}^{-1}$ . The instrumental velocity resolution, set by the slit width, was  $110 \text{ km s}^{-1}$ .

which seems a plausible scenario. A similar lag between the initial molecular gas concentrations and the appearance of H II regions was noted near the outer ends of the bar of NGC 7479 by Quillen et al. (1995).

The star formation rate, indicated by the size and brightness of the H II regions, increases toward the far ends of the bar. The brightest H II region complexes (labeled 2 and 4 in Fig. 1) and the largest concentration of CO (DRSR 1996) are found at the far western end of the bar. At the far ends of the  $x_1$  orbits, the stars and gas turn around (see the velocity diagrams by Athanassoula 1992), so the line-of-sight velocity is small (Figs. 1 & 3). The lower shock strength may be favourable for increased star formation. A lower shock strength at the far ends of the bar is indicated by the measured higher ratio of  $H\alpha / [NII] \approx 1$  to 1.5, as compared to the lower ratio of  $\approx 0.6$  near the first inner Lindblad resonance, where the shocks are strong (Fig. 1c).

### 3.5. Shock-excited, diffuse, ionized gas

Outside the galactic center, and outside the main H II regions is a faint, diffuse, ionized gas component seen in  $H\alpha$ , [NII], and [SII] (Fig. 1b). The diffuse emission is 20 to 50 times fainter than the emission of the H II regions. In the **diffuse** emission the  $H\alpha / [NII] 6583$  line ratio decreases gradually from  $\sim 1.5$  near both ends of the bar to  $\lesssim 0.6$  near the first inner Lindblad resonance (Fig. 1c). A similar decrease is observed for the line ratio  $H\alpha / [SII] 6716$ . In agreement with hydrodynamic models, the decrease in the  $H\alpha / [NII] 6583$  line ratio indicates an increasing shock strength toward the center. The CO study of DRSR (1996) found the highest molecular gas concentrations near the two positions where gas from the  $x_1$  orbit collides with gas on the  $x_2$  orbits, thereby producing the strongest shocks. For these regions we find the lowest ratio  $H\alpha / [NII] \approx 0.6$ . We do not find shocked diffuse gas near the far ends of the bar and inside the central plateau, probably because the strong emission of the H II regions swamps any faint emission from the diffuse ionized gas.

Could the faint emission detected in NGC 1530 be coming from diffuse ionized gas excited by photons leaking from H II regions into interstellar space? Although part of the observed diffuse emission may arise in this manner, it is evident from Fig. 1 that in NGC 1530 the faint emission is found at distances of  $\geq 1 \text{ kpc}$ , from prominent H II regions, where the density of leaked-out photons (i.e., the ionization parameter  $U$ ) should be

very small. Fig. 7 of Wang et al. (1997) shows for a selection of representative galaxies, that at distances  $> 200$  to  $300 \text{ pc}$  from H II regions the diffuse emission is very weak and the line ratio [NII]/ $H\alpha$  similar to the ratio observed in the diffuse emission of NGC 1530. As discussed by Martin (1997) and Rand (1998), the observed line ratios in the diffuse ionized emission at such large distances from H II regions can be explained only if there is a contribution from shock-excited gas.

We show in Fig. 7 three plots of diagnostic line ratios which substantiate our interpretation that the diffuse emission comes primarily from shock-excited gas. Fig. 7 (top panel) shows for NGC 1530 the [NII] 6583/ $H\alpha$  and [SII] 6716/ $H\alpha$  ratios versus the  $H\alpha$  intensity of the emitting region. This figure is similar to that obtained for NGC 891 by Rand (1998) and the galaxies studied by Wang et al. (1997). In NGC 1530 the diffuse emission comes from regions with  $H\alpha$  intensity  $\lesssim 50$ , in relative units, which is 20 to 50 times lower than the intensity from strong H II regions, such as those found in the  $x_2$  zone, inside the first inner Lindblad resonance. Fig. 7 (middle panel) shows the [SII]6716/[NII]6583 line ratios measured along the bar. This figure shows that there is a difference between the strong H II regions in the  $x_2$  zone and the diffuse gas in the  $x_1$  zones. Fig. 7 (bottom panel) shows the observed [NII]/ $H\alpha$  versus [SII]/ $H\alpha$  ratios. In this diagram, the emission from the H II region gas is at the lower left, while the diffuse emission is at the upper right, the region occupied by gas excited by shocks (see the shock model calculations by Dopita & Sutherland 1996). This feature is clearly evident in the observations of NGC 1530, and is especially remarkable near the first inner Lindblad resonance where gas associated with the  $x_1$  orbits collides with gas associated with the  $x_2$  orbits. This region is marked in Fig. 7 (middle and bottom panels) with the solid triangles, and is exactly the region of the shock-excited gas.

The [SII] 6716/6731 line ratio (Figs. 1 & 2) is fairly constant, with a value of 1.2 to 1.4 along both axes of the bar, and there is essentially no difference between the diffuse ionized gas and the H II regions (Figs. 1 & 2d). The ratio of 1.4 indicates that the sulfur ions are in the low-density regime (see Osterbrock 1989). This means that the upper limit on the electron density in the H II regions is  $n_e \approx 300 \text{ cm}^{-3}$ , about the same as the mean number density,  $n(H_2)$ , estimated for the molecular gas by DRSR (1996) and RD97. For the diffuse gas, however, the electron density must be much lower, in spite of the fact that the [SII] ratio is the same as in the H II regions. The line

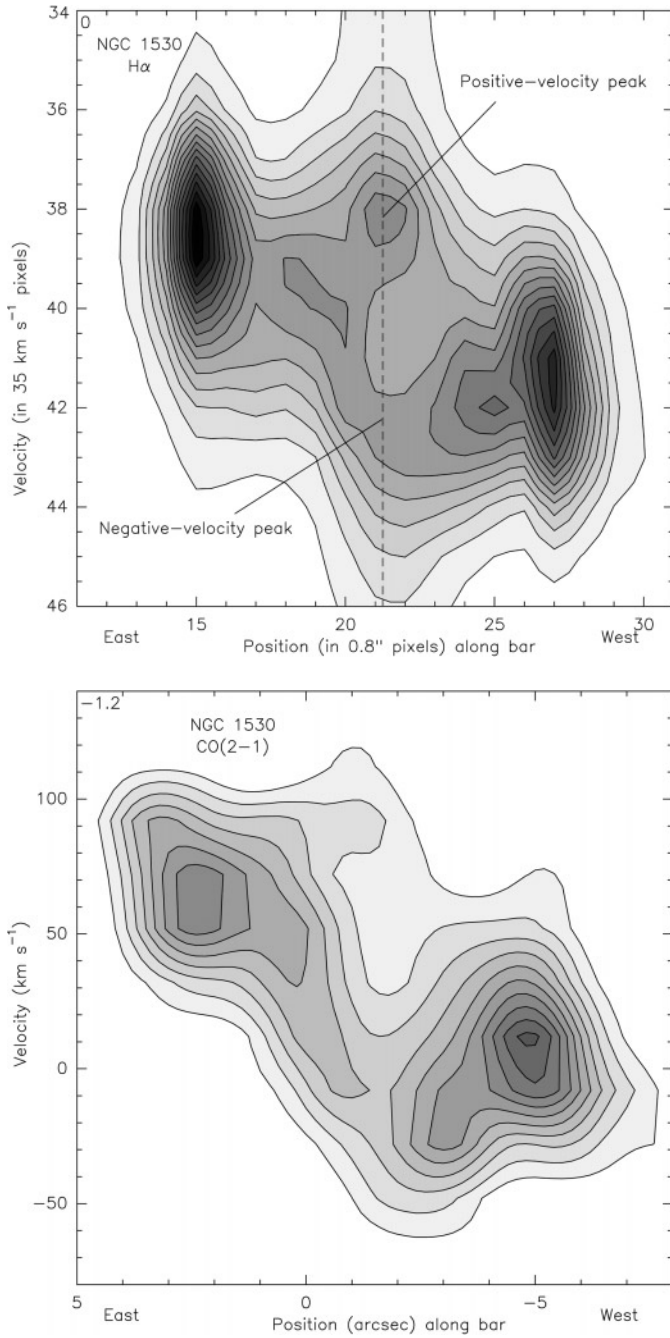


**Fig. 6.** Position-velocity diagrams along the bar, through the galactic center, cutting across the  $x_2$  orbits. *Upper:*  $H\alpha$  diagram, from the data in this paper. Slit width =  $1.5''$ , instrumental velocity resolution is  $110 \text{ km s}^{-1}$  (FWHM). The dashed vertical line shows the region of the twin-peaked spectra in the center of Fig. 5. *Lower:* CO(2–1) diagram, from data of Reynaud & Downes (1999). In the CO diagram, velocity offsets are relative to  $c z_{\text{lsr}} = 2450 \text{ km s}^{-1}$ . Beam =  $1.8'' \times 1.5''$ , velocity resolution  $20 \text{ km s}^{-1}$ . The zero position is  $04^{\text{h}}23^{\text{m}}27.32^{\text{s}}, +75^{\circ}17'45.0''$  (J2000).

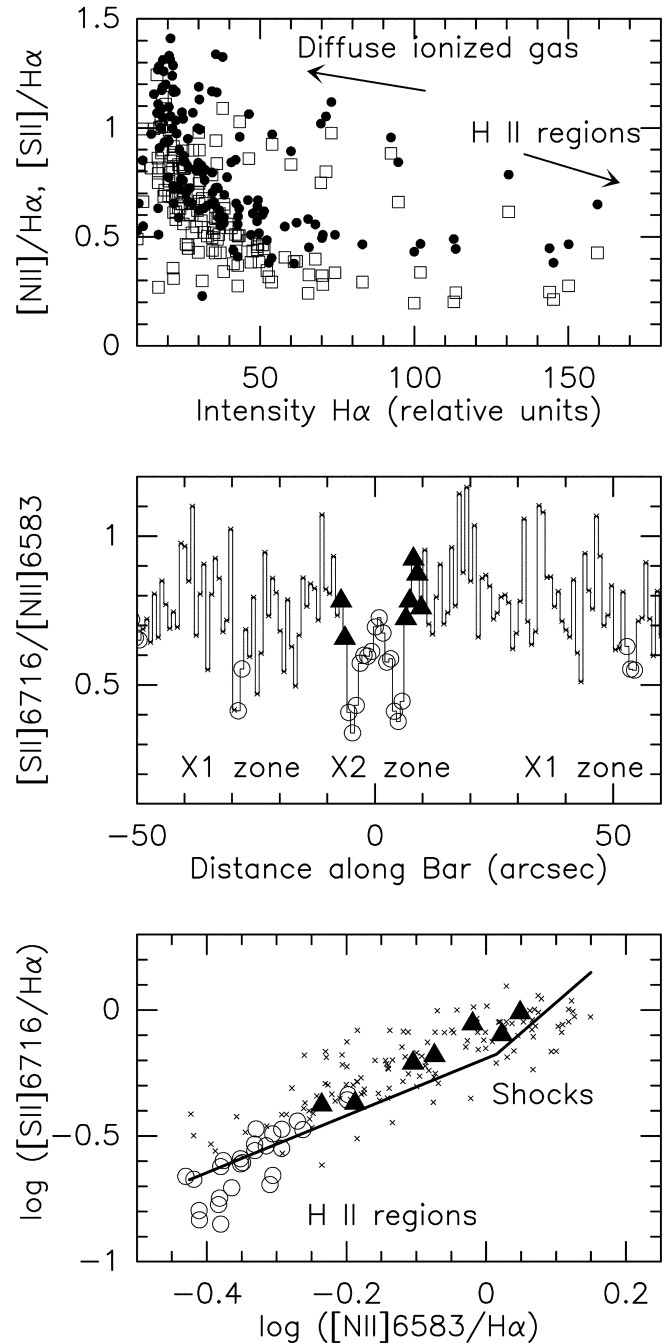


**Fig. 7.** Diagnostic line ratio diagrams for emission along the bar. (*Top:*) The ratios  $[\text{NII}]6583/H\alpha$  (solid dots) and  $[\text{SII}]6716/H\alpha$  (open squares) as a function of the  $H\alpha$  intensity of the emitting regions. The diffuse emission has a relative intensity  $\lesssim 50$ , which is 20 to 50 times weaker than the emission of the strongest H II regions (off scale to the right). (*Middle:*)  $[\text{SII}]6716/[\text{NII}]6583$  along the bar. Crosses = regions with relative  $H\alpha$  intensity  $< 50$ , i.e., regions of diffuse emission. Open circles = regions with intensities  $> 50$ , i.e., H II regions. Filled triangles = emission near the first inner Lindblad resonance. (*Bottom:*)  $[\text{SII}]/H\alpha$  versus  $[\text{NII}]/H\alpha$  ratios along the bar; the symbols are the same as in the middle panel. The solid line shows the fit for the diffuse ionized gas in NGC 891 (Rand 1998), which also has a contribution from shock-ionized gas.

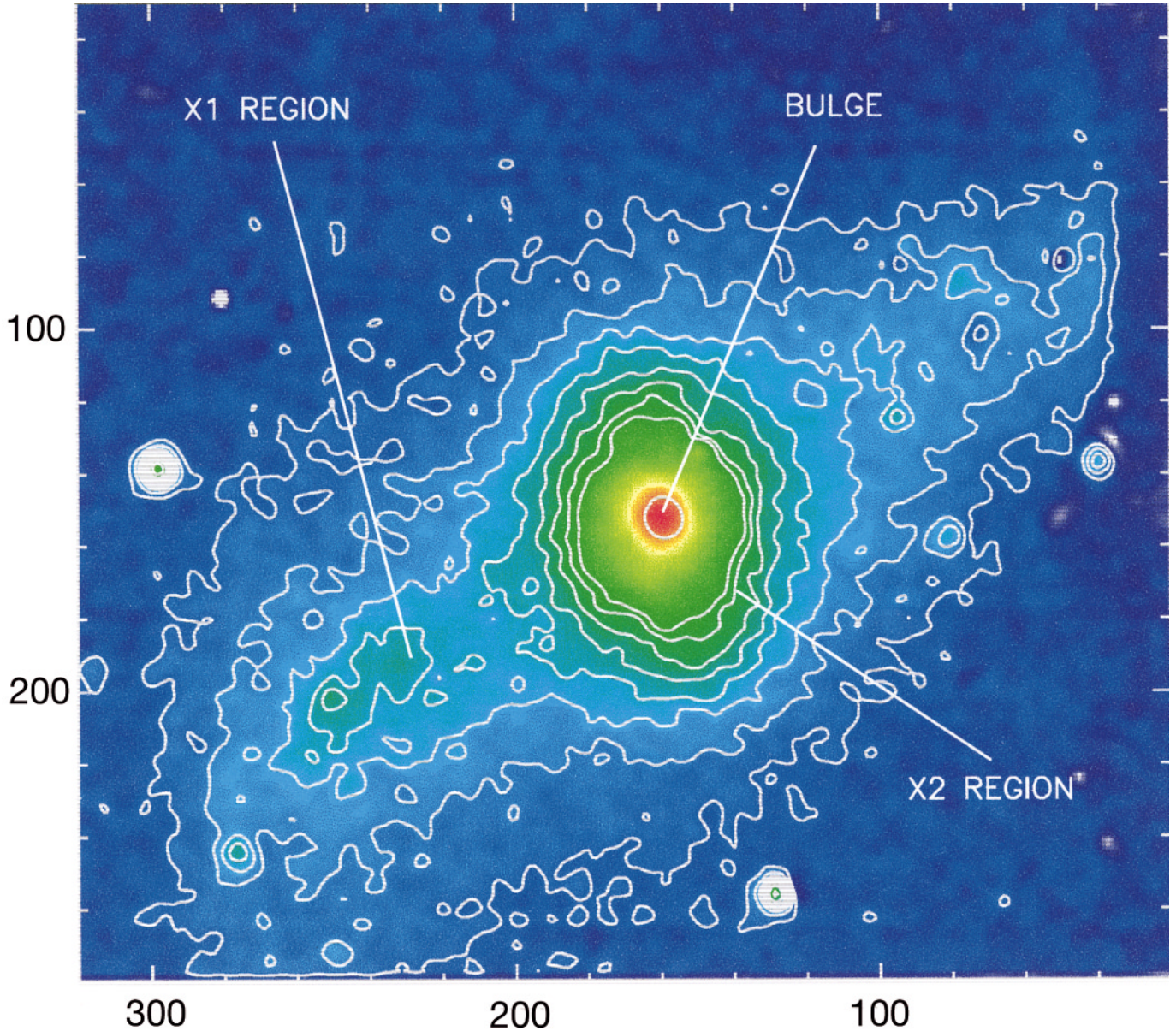


**Fig. 8.**  $I - B$  image showing the stellar surface brightness along the bar. Coordinates are  $0.8''$  pixels; north is up, east is left. Contours are 0.0125 to 0.125 by 0.0125 (the same relative units as Fig. 9). In these units, the peak at the bulge is 0.9 (top contour).

intensity of the diffuse gas is 20 to 50 times fainter than that of the H II regions, which indicates a lower column density in the same proportion. For comparable filling factors, this would imply an upper limit of  $n_e \approx 10 \text{ cm}^{-3}$  for the electron density of the diffuse, shocked gas, consistent with a pre-shock density of  $n_e \approx 1 \text{ to } 2 \text{ cm}^{-3}$ . Compression of the clouds to star-forming densities occurs when further cooling behind the shock allows the clouds to contract under their own gravity.

#### 4. Results on the stellar distribution

We used an  $I - B$  image of NGC 1530, that is nearly free of emission from OB stars and H II regions (Fig. 8), to trace the

distribution of the populations that contain most of the stellar mass. The stellar brightness distributions of bulge, the  $x_1$  zone, and the  $x_2$  orbit zone differ greatly in intensity and in the shape of their radial profile. The results are shown in Fig. 9.

##### 4.1. The nuclear bulge ( $r \leq 0.5 \text{ kpc}$ )

In the units of Fig. 9a, the relative surface brightness of the nuclear bulge stars is  $B_b(r) = 0.9 \text{ to } 1.0$  for  $r \leq 0.5 \text{ kpc}$ . The nuclear bulge surface brightness is constant out to the radius where the angular velocity ( $\Omega - \kappa/2$ ) has a maximum (RD97), and where we observe the twin peaks in the H $\alpha$  profiles (see above).

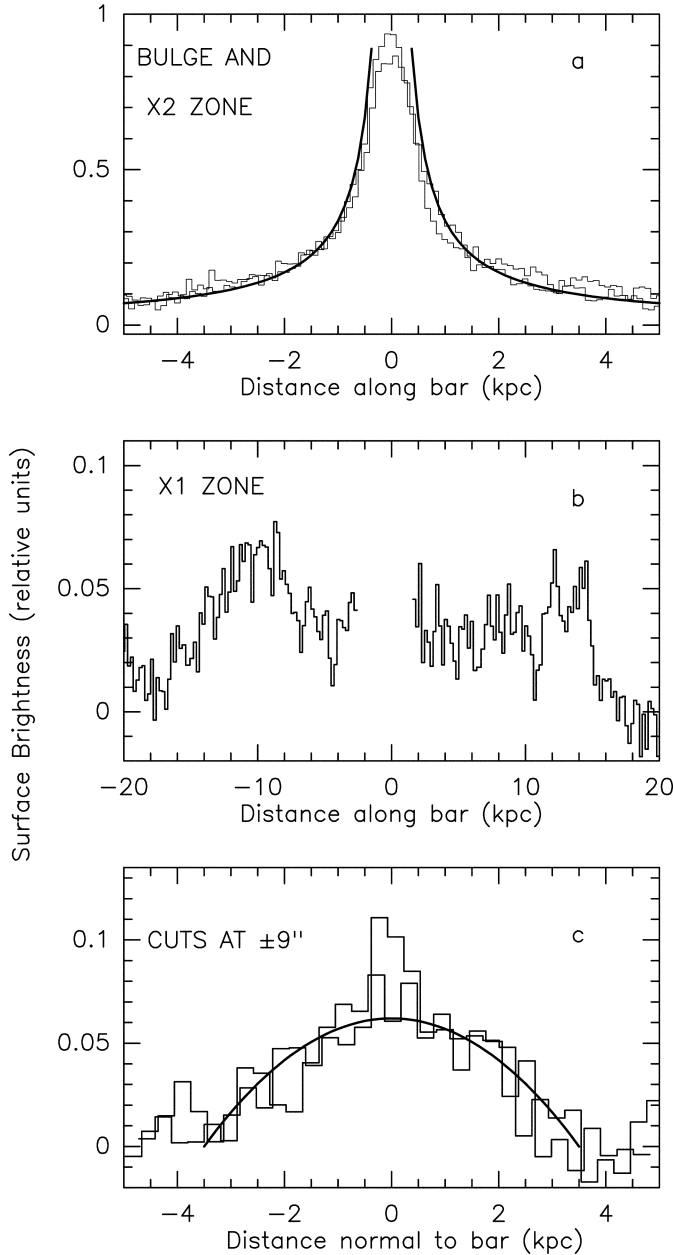


**Fig. 9.** **a:** Surface brightness in the central zone (stars in the nuclear bulge and stars on  $x_2$  orbits). The histograms are tracings along and perpendicular to the bar. The heavy curves trace  $L(r) \propto 0.3/r$ . **b:** Surface brightness along the bar, minus the brightness distributions of the nuclear bulge and the  $x_2$  orbit stars (see **a**). **c:** Surface brightness at radii of  $\pm 9$  kpc from the center, plotted against distance normal to the bar. The heavy curve traces  $L(d) \propto 1/d^2$ .

#### 4.2. The $x_2$ orbit stars ( $0.5 \leq r \leq 2$ kpc)

Fig. 9a shows the stellar surface brightness of the central region containing the  $x_2$  orbits. The relative surface brightness of the  $x_2$  orbit zone is  $B_{x_2}(r) \approx 0.3/r$  for  $0.5 \text{ kpc} \lesssim r \lesssim 2 \text{ kpc}$ , where  $r$  is the radius in kpc. The  $x_2$  orbits extend out to the first inner Lindblad resonance (Fig. 9a). In deprojected, linear units, the tracings along and perpendicular to the bar are nearly the same.

Hence, the surface brightness of the  $x_2$  orbit region is radially symmetric, which means that the shapes of the  $x_2$  orbits are closer to circles than to ellipses.

#### 4.3. The $x_1$ orbit stars ( $2 \text{ kpc} \leq r \leq 12 \text{ kpc}$ )

The stars of the  $x_1$  orbits move in a bar  $\sim 28$  kpc long. Fig. 9b shows the stellar surface brightness along the bar, minus the brightness distribution of the  $x_2$  orbit stars (Fig. 9a). The stellar surface brightness of the  $x_1$  orbit zone is 1/10th that of the  $x_2$  orbit zone and the central bulge (Fig. 9a and b). Fig. 9c shows the brightness distribution on cuts *perpendicular* to the major axis of the bar, at radii of  $\pm 9$  kpc from the center. Perpendicular cuts at other radii are similar. The surface brightness perpendicular to the bar falls off as  $d^{-2}$ , with a full width to half maximum of  $\sim 4$  kpc (Fig. 9c).

## 5. Estimates of the mass of stars

### 5.1. Dynamical mass estimated from rotation velocities

Near the first inner Lindblad resonance ( $r \approx 1.8$  kpc) the rotation velocity of the gas is  $200 \text{ km s}^{-1}$  (for a galaxy inclination of  $55^\circ$ ). Hence the dynamical mass in stars and gas interior to  $r = 1.8$  kpc, the radius where the  $x_2$  zone disappears on the  $I - B$  image, is

$$M(\text{bulge} + x_2) \approx rv^2/G \approx 1.7 \times 10^{10} M_\odot, \quad (1)$$

This central zone contains  $6 \times 10^9 M_\odot$  in molecular gas (DRSR 96), so subtracting this gas mass from the dynamical mass yields a mass of the bulge plus  $x_2$  stars of  $1.1 \times 10^{10} M_\odot$ . (In this circumnuclear region, we neglect the contribution of the galactic halo.)

At the ends of the bar, at  $r = 14$  kpc, the rotation velocity of the gas is  $200 \text{ km s}^{-1}$ . Hence the dynamical mass interior to  $r = 14$  kpc is

$$M(r \leq 14 \text{ kpc}) \approx rv^2/G \approx 1.3 \times 10^{11} M_\odot, \quad (2)$$

This dynamical mass is the mass of all the gas and stars in the nucleus, the bar, and in the much fainter stellar disk and dark halo surrounding the bar. This zone contains  $1 \times 10^{10} M_\odot$  in molecular gas (DRSR 96).

### 5.2. Stellar mass ratios derived from brightness distributions

We integrated the relative surface brightness over the area of the bulge and the  $x_1$  and  $x_2$  orbits to obtain  $L(\text{bulge})$ ,  $L(x_1)$ , and  $L(x_2)$ . In the relative intensity units of Fig. 9, the surface brightness integrals yield

$$L(\text{bulge}) \approx 0.9 \times \pi(0.5 \text{ kpc})^2 \approx 0.7 \quad (3)$$

$$L(x_2) \approx \int_{0.5 \text{ kpc}}^{1.8 \text{ kpc}} (0.3/r) 2\pi r dr \approx 2.4 \quad (4)$$

In the units of Fig. 9, the relative surface brightness of the  $x_1$  stars is 0.05 units (see Fig. 9 b,c). The integrated surface brightness of the  $x_1$  orbit stars is then:

$$L(x_1) \approx 0.05(\ell \times b) \approx 4.8, \quad (5)$$

**Table 1.** Mass distribution in NGC 1530.

<b>Stars</b>	radius (kpc)	luminosity rel.bulge+ $x_2$	Mass ( $M_\odot$ )	Percent of whole galaxy
Bulge stars	0.5	0.22	$2.4 \times 10^9$	0.7 %
$x_2$ zone stars	1.8	0.78	$8.6 \times 10^9$	2.7 %
Bulge + $x_2$ stars	1.8	<b>(1.00)</b>	<b>(<math>1.1 \times 10^{10}</math>)</b> <sup>a</sup>	3.4 %
$x_1$ zone stars	14.0	1.55	$1.7 \times 10^{10}$	5.3 %
Bulge + $x_2$ + $x_1$	14.0	2.55	$2.8 \times 10^{10}$	8.7 %
<b>Gas</b>	radius (kpc)		Mass ( $M_\odot$ )	Percent of whole galaxy
$x_2$ region gas	1.8	–	$6 \times 10^9$	1.9 %
$x_1$ region gas	14	–	$4 \times 10^9$	1.3 %
Bar gas ( $x_1 + x_2$ )	14	–	$1 \times 10^{10}$	3.2 %
H I gas	34	–	$1.7 \times 10^{10}$	5.2 %
H I + H <sub>2</sub> + He	34	–	$2.7 \times 10^{10}$	8.4 %
<b>Dynamical Mass</b>	radius (kpc)	rot. vel. ( $\text{km s}^{-1}$ )	Mass ( $M_\odot$ )	Percent of whole galaxy
Bulge region	0.5	140	$2.3 \times 10^9$	0.7%
$x_2$ zone	1.8	200	$1.7 \times 10^{10}$	5.3%
whole bar	14	200	$1.3 \times 10^{11}$	41.2%
<b>whole galaxy</b>	34	200	$3.2 \times 10^{11}$	100.0%

<sup>a</sup> Adopted mass for scaling relative luminosities.

with  $\ell \approx 24$  kpc the effective length of the bar (minus the  $x_2$  region) and  $b \approx 4$  kpc the full width to half maximum of the bar. We thus find  $L(x_1)/L(\text{bulge} + x_2) \approx 4.8/3.1 = 1.5$ . If the surface brightness is proportional to the number of stars on the line-of-sight, and if the mass-to-luminosity ratios of the bulge and  $x_1$  and  $x_2$  orbit stars are the same, then the ratio of numbers of stars in the  $x_1$  orbits and bulge and  $x_2$  orbits is also  $\approx 1.5$ . From the total dynamical mass of the nuclear bulge plus  $x_2$  orbit stars  $M(\text{bulge} + x_2) \approx 1.1 \times 10^{10} M_\odot$  derived from the CO rotation curve (see above), we obtain  $M(x_1) \approx 1.7 \times 10^{10} M_\odot$  for the total mass of the  $x_1$  orbit stars. Similarly, the mass of the stars in the central bulge of radius 0.5 kpc (where the surface brightness is constant) is

$$M_b \approx [L_b / L(\text{bulge} + x_2)] M(\text{bulge} + x_2) \quad (6)$$

$\approx (0.7/3.1) \times 1.1 \times 10^{10} M_\odot = 2.4 \times 10^9 M_\odot$ . This agrees with the mass used in the dynamical calculations of RD97. The results of these estimates are summarized in Table 1; the uncertainties are of the order of 20 to 30 %.

### 5.3. Mass distribution of gas and stars

The total dynamical mass of the whole galaxy, estimated from the H I rotation curve (Regan et al. 1996) out to a radius of 34 kpc from the galactic center, is  $3.2 \times 10^{11} M_\odot$ . Of this total mass, 3% is in the stars in the  $x_2$  orbits (the inner Lindblad resonance), 5% is in the stars in  $x_1$  orbits (the bar), and 1% is in the nuclear bulge. Another 3%, or  $1 \times 10^{10} M_\odot$ , is in the molecular gas within  $r = 14$  kpc (DRSR 1996). Within this region, there appears to be no detectable atomic hydrogen gas

(Regan et al. 1996). The “bar”, meaning the bulge, the  $x_2$  and  $x_1$  stars, and the molecular gas in the bar, thus contain  $4 \times 10^{10} M_\odot$ , or 30% of the dynamical mass within  $r = 14$  kpc. The remaining 70% of the dynamical mass within a 14 kpc radius must be made up of stars in the much fainter disk surrounding the bar plus the dark halo matter, out of the disk plane. Relative to the whole galaxy, the stars and gas in the bar make up 12% of the total mass.

## 6. Conclusions

- 1) Our analysis of long slit spectra along and perpendicular to the bar of the galaxy NGC 1530 shows that the H II regions have the same kinematics as the molecular gas.
- 2) The measured spatial variation of the H $\alpha$  and [NII] line intensity is consistent with the distribution of molecular gas along the dust lanes and its high concentration in the  $x_2$  orbits, near the center of the galaxy.
- 3) The most intense H II regions are in a well-defined ring at the inner Lindblad resonance, at a radius of 1.4 kpc from the galactic center.
- 4) Along the bar, the H II regions are in the post-shock zone, slightly downstream of the dust lanes that contain molecular gas.
- 5) Beyond the H II regions in the bar is faint, diffuse, ionized gas with low H $\alpha$  / [NII] and H $\alpha$  / [SII] line ratios, which confirm the presence of shocks in the bar and supports a shock origin of the dust lanes.
- 6) The [SII] line ratios are constant and equal to  $\sim 1.2$ – $1.4$ , the low-density limit, throughout the bar. This implies the mean

electron densities in the H II regions are  $< 300 \text{ cm}^{-3}$ . From the ratio of the line intensities, we estimate that the electron densities in the shocked, diffuse ionized gas are  $\lesssim 10 \text{ cm}^{-3}$ , and  $\lesssim 1$  to  $2 \text{ cm}^{-3}$  in the diffuse, pre-shock gas.

7) We derive from an  $I - B$  image the surface brightness along the bar which we interpret as the stellar distribution. We use these data to estimate the mass in the various structural components in the bar. The mass of the stars and gas in the bar is  $4 \cdot 10^{10} M_{\odot}$ , or 12% of the total mass of the galaxy.

*Acknowledgements.* These results are based on service observations made with the Isaac Newton Telescope (INT) operated on the Island of La Palma by the INT Group in the Spanish Observatorio de Roque de los Muchachos of the Instituto de Astrofísica de Canarias, and observations made at the Calar Alto Observatory, Spain. We thank Dr. C. Benn (RGO) for taking the spectra with the INT on La Palma. We thank the referee Dr. H. Kristen, and the second, anonymous, referee, for their helpful comments.

## References

- Athanassoula E., 1992, MNRAS 259, 345  
 Beck R., Ehle M., Shoutenkov V., Shukurov A., Sokoloff D., 1999, Nat 397, 324  
 Burbidge E.M., Burbidge G.R., 1962, ApJ 135, 694  
 Burbidge E.M., Burbidge G.R., 1965, ApJ 142, 634  
 Burbidge E.M., Gould R.J., Pottasch S.R., 1963, ApJ 138, 945  
 Condon J.J., Helou G., Sanders D.B., Soifer B.T., 1996, ApJS 103, 81  
 Contopoulos G., Mertzaniades C., 1977, A&A 61, 477  
 Dopita M.A., Sutherland R.S., 1995, ApJ 455, 468  
 Dopita M.A., Sutherland R.S., 1996, ApJS 102, 161  
 Downes D., Reynaud D., Solomon P., Radford S.J.E., 1996, ApJ 461, 186 (**DRSR**)  
 Duval M.F., 1977, Ap&SS 48, 103  
 Englmaier P., Gerhard O., 1997, MNRAS 287, 57  
 Grosbol P., 1985, A&AS 60, 261  
 Koribalski B., 1996, In: Skillman E.D. (ed.) Minnesota Lectures on Extragalactic Neutral Hydrogen. ASP Conf. Series, ASP, San Francisco, p. 238  
 Lindblad P.O., Hjelm M., Högbom J., et al., 1996a, A&AS 120, 403  
 Lindblad P.A.B., Lindblad P.O., Athanassoula E., 1996b, A&A 313, 65  
 Lindblad P.A.B., Kristen H., 1996, A&A 313, 733  
 Marquez I., Moles M., Masegosa J., 1996, A&A 310, 401  
 Martin C.L., 1997, ApJ 491, 561  
 Morse J.A., Raymond J.C., Wilson A.S., 1996, PASP 108, 426  
 Ondrechen M.P., 1985, AJ 90, 1474  
 Ondrechen M.P., van der Hulst J.M., 1983, ApJ 269, L 47  
 Osterbrock D.E., 1989, Astrophysics of Gaseous Nebulae and Active Galactic Nuclei. University Science Books, Mill Valley, California, 134  
 Pence W.D., Blackman C.P., 1984, MNRAS 207, 9  
 Piner B.G., Stone J.M., Teuben P.J., 1995, ApJ 449, 508  
 Quillen A.C., Frogel J.A., Kenney J.D., Pogge R.W., DePree D.L., 1995, ApJ 441, 549  
 Rand R.J., 1998, ApJ 501, 137  
 Regan M.W., Vogel S.N., Teuben P.J., 1995, ApJ 449, 576  
 Regan M.W., Teuben P.J., Vogel S.N., van der Hulst T., 1996, AJ 112, 2549  
 Regan M.W., Vogel S.N., Teuben P.J., 1997, ApJ 484, L143  
 Reynaud D., Downes D., 1997, A&A 319, 737 (**RD97**)  
 Reynaud D., Downes D., 1998, A&A 337, 671 (**RD98**)  
 Reynaud D., Downes D., 1999, A&A, submitted  
 Roberts W.W., Huntley J.M., van Albada G.D., 1979, ApJ 233, 67  
 Rubin V.C., Ford W.K., Thonnard N., 1980, ApJ 238, 471  
 Sandqvist Aa., Jörsäter S., Lindblad P.O., 1995, A&A 295, 585  
 Storchi-Bergman T., Wilson A.S., Baldwin J.A., 1996, ApJ 460, 252  
 Vega Beltrán J.C., Zeilinger W.W., Amico P., et al., 1998, A&AS 131, 105  
 Wang J., Heckman T.M., Lehnert M.D., 1997, ApJ 491, 114  
 Weiner B.J., Williams T.B., Sellwood J.A., 1993, BAAS 25, 1411  
 Weiner B.J., Sellwood J.A., Williams T.B., 1996, In: Buta R., Crocker D.A., Elmegreen B.G. (eds.) Barred Galaxies. ASP Conf. Series 91, San Francisco, 489